GSA Data Repository 2016197

Supplementary materials for: Dynamic weakening and amorphisation during laboratory earthquakes in serpentinite

Nicolas Brantut[1], François X. Passelègue[2], Damien Deldicque[2]
Jean-Noël Rouzaud[2] & Alexandre Schubnel[2]

[1] *Rock & Ice Physics Laboratory and Seismological Laboratory, Department of Earth Sciences, University College London, Gower Street, London, WC1E 6BT, UK.*
[2] *Laboratoire de Géologie, CNRS UMR 8538, École Normale Supérieure, 24 rue Lhomond, 75005 Paris, France.*

1 Estimation of Rupture Speed

Arrival times were picked automatically form the raw waveforms using a method based on the Akaike Information Criterion, with a precision (checked by comparing with manual picks) of the order of 1 μs. The forward problem consists in a simple model for the rupture front arrival time, in which the rupture is assumed to be either circular (for sub-Rayleigh rupture speeds) or elliptical (for super-shear rupture speeds). The theoretical arrival time at station i, denoted t_i, is computed as

$$t_i = t_0 + \sqrt{\frac{(x-x_i)^2}{c_{III}^2} + \frac{(y-y_i)^2}{c_{II}^2}}, \tag{1}$$

where t_0 is the origin time of the rupture, (x,y) are the coordinates of its initiation point in the fault plane, c_{II} (resp. c_{III}) is the rupture speed in the in-plane (resp. out of plane) direction, and (x_i,y_i) are the coordinates of the station. The inverse problem consists in determining the model parameters x, y, t_0, c_{II}, and c_{III}. We used a generic grid-search approach, sweeping through all potential values for each parameter, and computing a likelihood function based on the least absolute value criterion. For simplicity we assumed a circular rupture front ($c_{II} = c_{III}$) for sub-Rayleigh ruptures ($c_{II} < c_s$), and assumed that $c_{III} = c_s$ during supershear ruptures. In the inversion we used a constant value of the shear wave speed $c_s = 3.83$ km/s.

2 Supplementary Figures

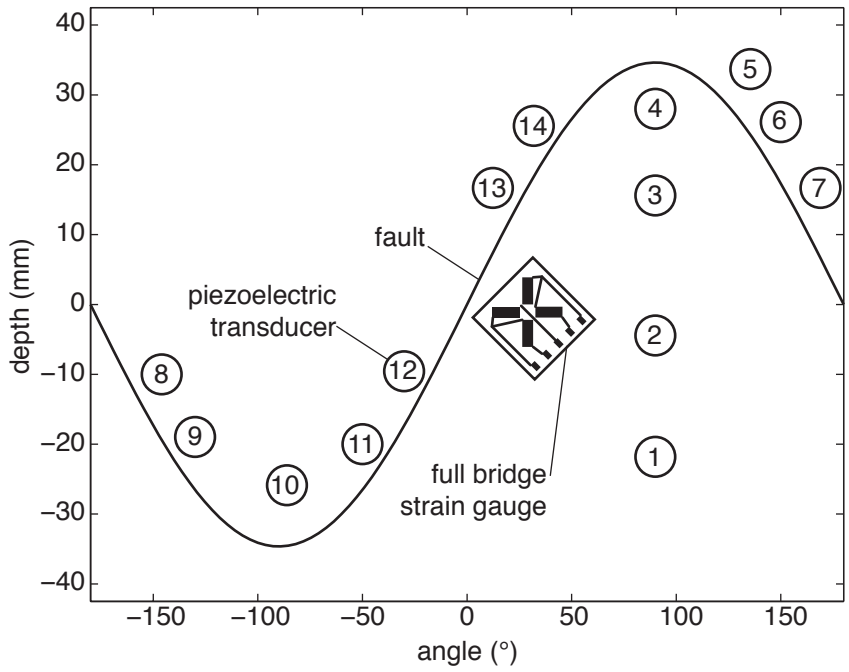

Figure DR1: Schematic of the sensor arrangement and strain gauge positioning around the sample. The sensor positions for the samples deformed at 95 and 30 MPa confining pressure were almost identical, with minor variations due to the manual fabrication of the perforated jacket

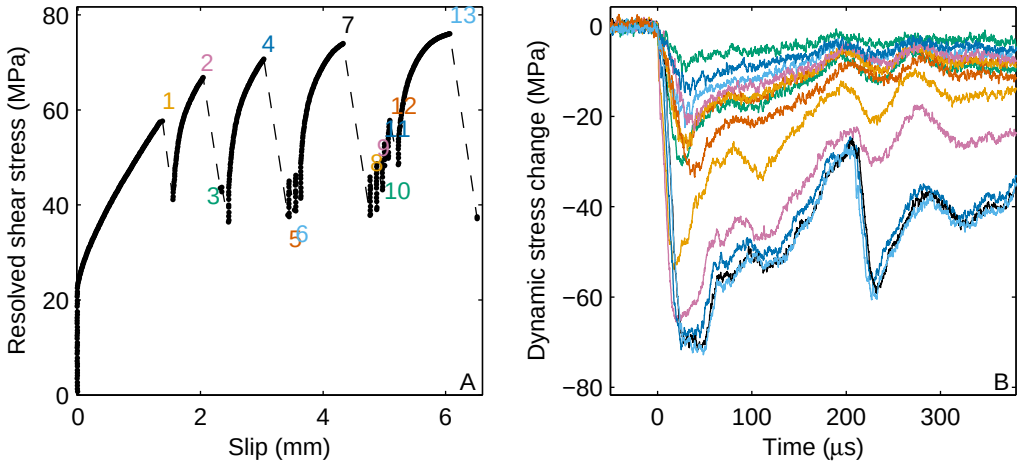

Figure DR2: Stick-slip events during antigorite friction at a confining pressure of 30 MPa. (A) Resolved shear stress as a function of slip displacement along the simulated fault in antigorite. The dashed lines correspond to stick-slip events, during which stress drops and slip is too rapid to be captured by the low frequency (1 Hz) recording of the data. (B) Records of dynamic stress changes during each stick slip event, recorded at 10 MHz from a strain gauge bridge positioned near the fault. Numbers and colors correspond to the events marked in panel A.

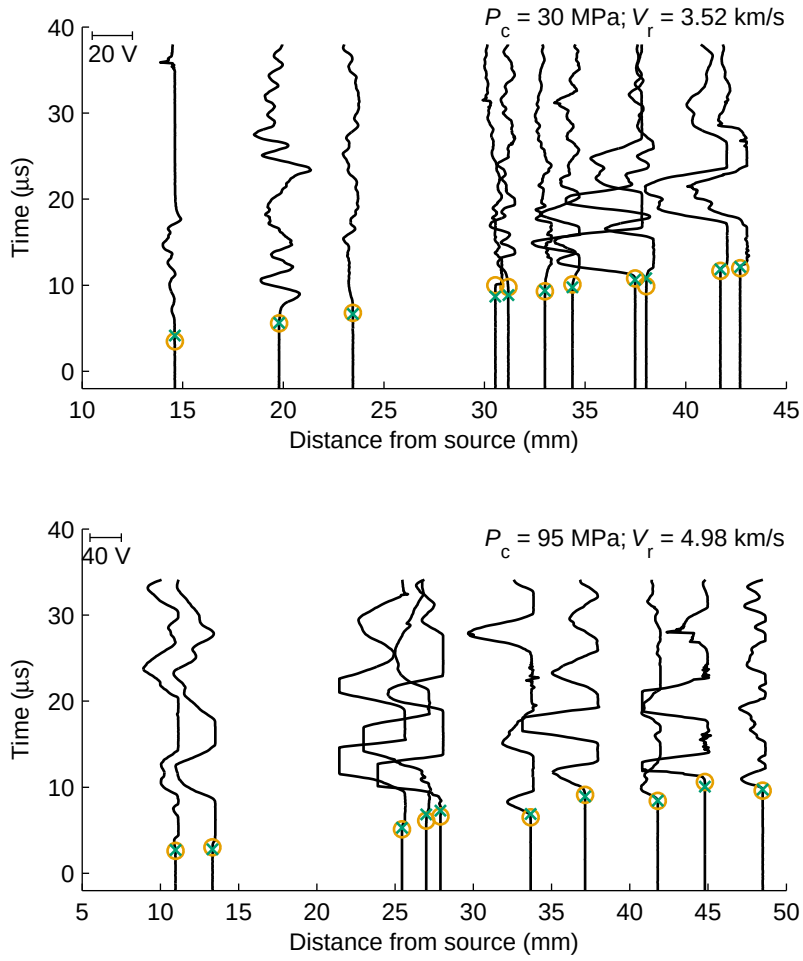

Figure DR3: Representative examples of waveforms recorded on the piezoeletric transducers during two stick-slip events, which were inferred to propagate at subshear (top) and supershear (bottom) rupture speeds. Orange circles mark picked rupture arrival times, and green crosses mark computed theoretical arrival times. Traces for each sensor are plotted as a function of the distance to the source location.

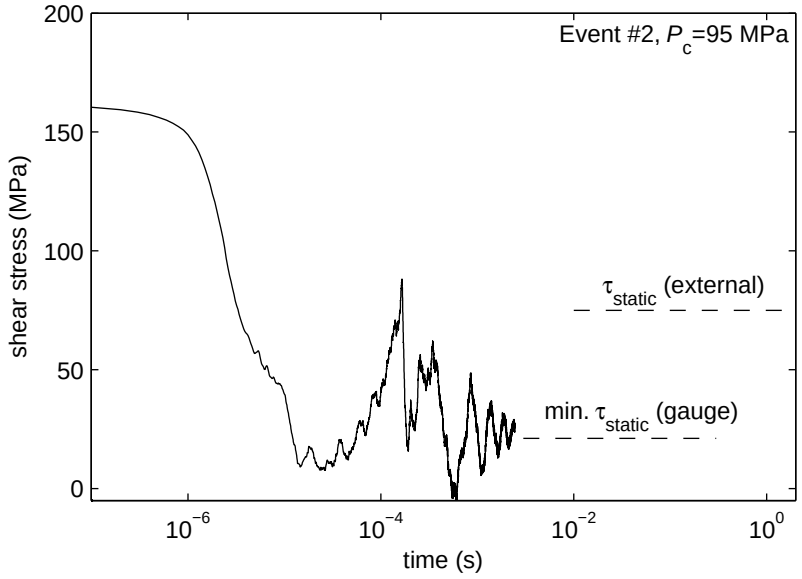

Figure DR4: Representative example of a full length stress-time time record, corresponding to event number 2 recorded in the experiment performed at $P_c = 95$ MPa. The dashed line marked with τ_{static} (gauge) corresponds to the stress level measured by the full bridge strain gauge immediately after the rupture event, recorded at a 10 Hz sampling rate. The dashed line marked with τ_{static} (external) corresponds to the stress level measured externally at the end of the loading column, recorded at 1 Hz.

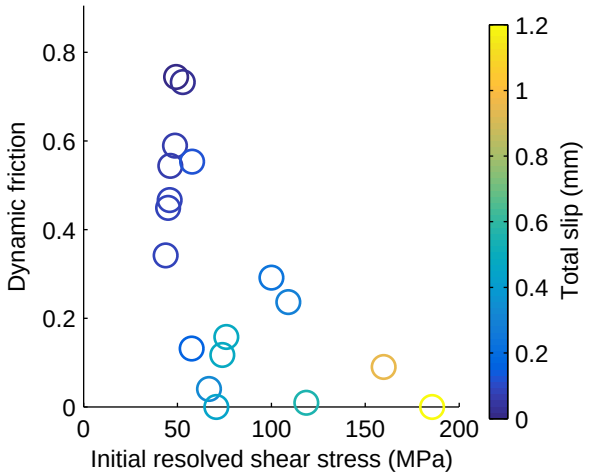

Figure DR5: Dynamic friction coefficient as a function of the initial resolved shear stress on the fault plane immmediately prior to stick-slip events. There is a clear trend towards decreasing (and even vanishing) dynamic friction coefficient with increasing initial shear stress.

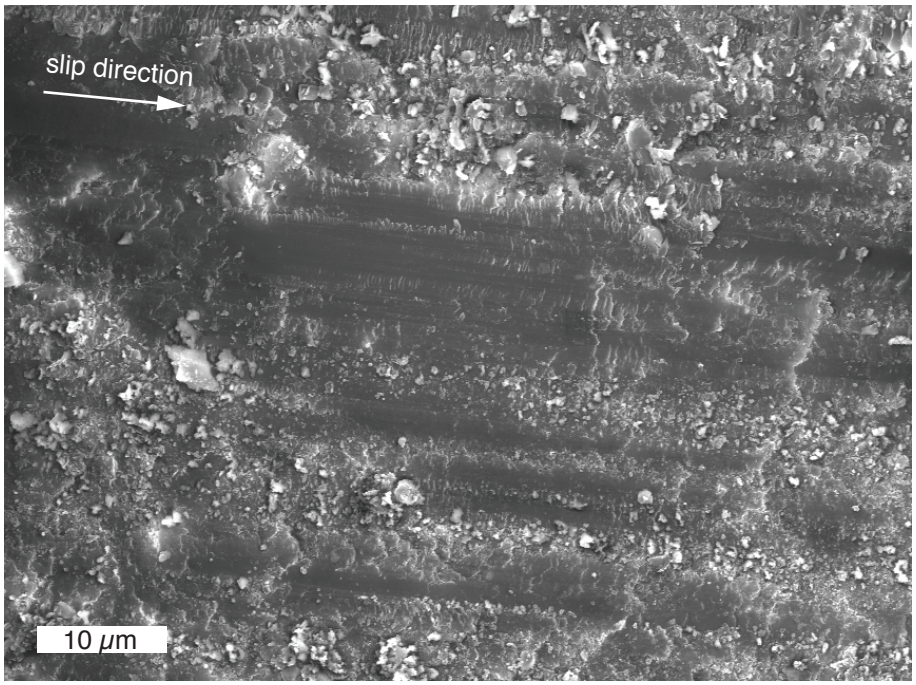

Figure DR6: SEM secondary electron image of the sliding surface of a pre-cut antigorite sample deformed at 60 MPa confining pressure but unloaded before any stick-slip event occurred. The surface texture is markedly different from that observed after stick-slip events, and shown only grooving and grain size reduction. No foam-like material or flow structures could be observed.

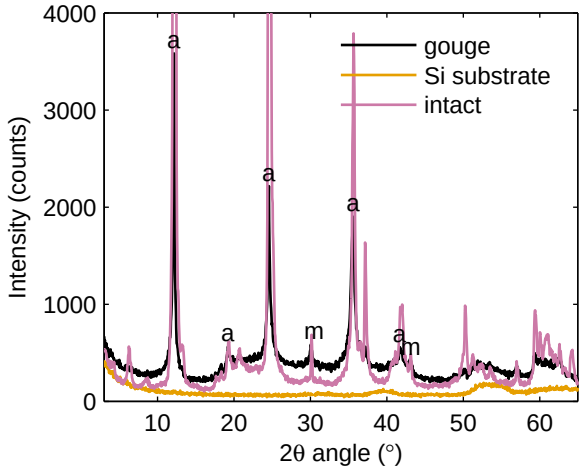

Figure DR7: X-ray powder diffraction pattern of the collected surface gouge after the experiment at 95 MPa confining pressure. The gouge was collected by shaking one half of the faulted sample in an alcohol bath using ultrasounds, and letting the alcohol evaporate from the bath. No further grinding was used. The measurement was performed using a silicon substrate. Antigorite peaks (a), as well as magnetite peaks (m; already present in the intact material) appear very clearly, but no significant other crystalline phase can be detected. By contrast with both the Si substrate alone (shown in orange) and the intact antigorite (shown in pink), the gouge pattern also contains a clear bump between 15 and 45 degrees, which indicates the presence of amorphous material.

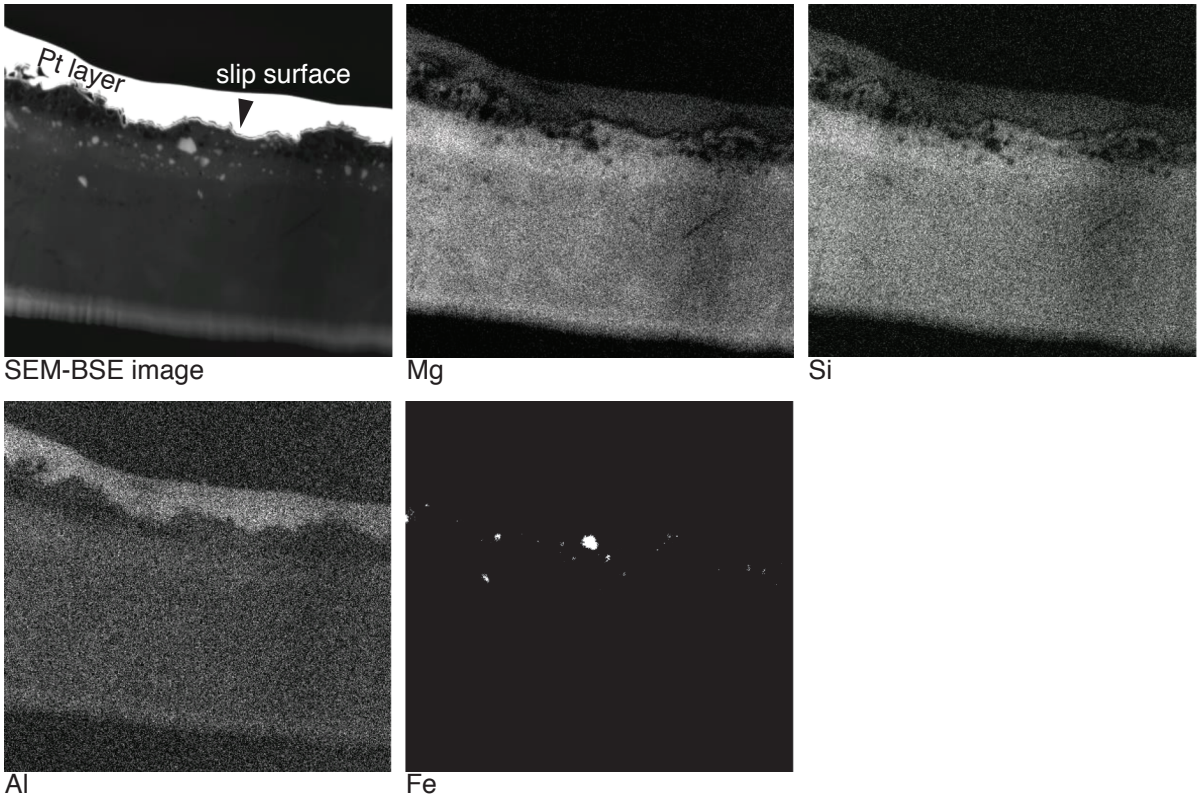

Figure DR8: Chemical composition analysis of the FIB section using energy dispersive x-ray spectroscopy under the SEM. The top left image is a backscattered electron image of the section, and the other images are elemental maps of magnesium (Mg), silicon (Si), aluminum (Al) and iron (Fe). The relative abundance of each element is indicated by the color scale, from black (element is absent) to white (very abundant). There is a distinct layer beneath the slip surface in which all major elements are more abundant than below, which indicates a lower concentration in oxygen, which can be explained by devolatilisation of structural water from the initial antigorite.